Comparative Study between the 3D-Liver Spheroid Models Developed from HepG2 and Immortalized Hepatocyte-Like Cells with Primary Hepatic Stellate Coculture for Drug Metabolism Analysis and Anticancer Drug Screening

Arunsajee Sae-be, Teerawat Wiwatpanit, Thaveechai Varatthan, Thanaphon Namporn, Sasiwat Laungkulldej, Ratthiya Thiabma, Atchara Jaiboonma, Khanit Sa-ngiamsuntorn, Daniel Elson, Alexandra E. Porter, Korbtham Sathirakul, Suradej Hongeng,* and Pakatip Ruenraroengsak*

Liver spheroids may be the best alternative models for evaluating efficacy and toxicity of the new anticancer candidates and diagnostics for hepatocellular carcinoma (HCC). Here, novel 3D-liver spheroid models are constructed from human hepatoma cells (HepG2)/ immortalized human hepatocyte-like cells (imHCs) with primary hepatic stellate cells (HSCs) coculture using the ultralow attachment technique. Spheroid morphology, HSC distribution, metabolic activity, protein expressions, and drug penetration are evaluated. All developed 3D spheroid models exhibit in spherical shape with narrow size distribution, diameter between 639–743 (HepG2-10%HSC) and 519–631 (imHC-10%HSC) μm. Both imHC mono and coculture models significantly express normal liver biomarkers at the higher level than HepG2 models. While 3D-HepG2 models significantly exhibit HCC biomarkers at the higher level than imHC models. HepG2 and imHC spheroids express basal cytochrom P450 (CYP450) enzymes at different levels depending on cell types, culture period, and ratio of coculture. Their metabolic activities for dextromethorphan (CYP2D6) tolbutamide (CYP2C9) and midazolam (CYP3A4) are routinely evaluated. For midazolam metabolism, imHC models allow the detection of phase II metabolic enzymes (UGT2B4 and UGT2B7). The presence of HSC in HepG2-HSC model increases biological barrier for doxorubicin (DOX) penetration, and escalates IC_{50} of DOX from 61.4 to 127.2 μg mL^{-1}.

1. Introduction

Liver cancer is currently the third leading cause of cancer-related death with over 900000 new cases diagnosed worldwide in 2020.[1] Hepatocellular carcinoma (HCC) is a major primary liver cancer worldwide accounting for approximately 75%–80% of all cases.[2] Several studies have revealed that the 2D cancer model failed to recapitulate the complexity of solid tumor and their microenvironment causing the low success rate, approximately 5%, of new anticancer entities in clinical studies.[3] Furthermore, the discrepancy between in vitro and in vivo of the traditional 2D culture models has provoked the development of an alternative in vitro model for anticancer drug screening.

Over the past decades, in vitro 2D liver models have played a vital role in drug discovery and drug development processes including the analysis of pharmacokinetics, pharmacological, and toxicological profiles. 2D-primary human hepatocytes (2D-PHHs) have been considered as the gold standard in vitro model for drug-induced

A. Sae-be, T. Namporn, S. Laungkulldej, K. Sathirakul, P. Ruenraroengsak
Department of Pharmacy
Faculty of Pharmacy
Mahidol University
447 Sri-Ayutthaya Rd, Rajathevi, Bangkok 10400, Thailand
E-mail: pakatip.rue@mahidol.ac.th; pakatip.rue@mahidol.edu

The ORCID identification number(s) for the author(s) of this article can be found under https://doi.org/10.1002/adtp.202200169

T. Wiwatpanit, T. Varatthan, R. Thiabma, A. Jaiboonma
National Center for Genetic Engineering and Biotechnology (BIOTEC)
National Science and Technology Development Agency (NSTDA)
Pathum Thani 10200, Thailand

S. Hongeng
Department of Pediatrics
Faculty of Medicine Ramathibodi Hospital
Mahidol University
Rama VI Rd, Rajathevi, Bangkok 10400, Thailand
E-mail: suradej.hon@mahidol.ac.th

K. Sa-ngiamsuntorn
Department of Biochemistry
Faculty of Pharmacy
Mahidol University
447 Sri-Ayutthaya Rd, Rajathevi, Bangkok 10400, Thailand

hepatoxicity analysis because they reflect the native phenotypes and functions of the normal human liver.[4–5] In addition, the U.S. FDA has recommended the utilization of the 2D-PHH culture as a practical model for in vitro drug interaction studies.[6] However, the drawbacks of the conventional 2D-PHHs include the de-differentiation, the rapid loss of hepatocyte-specific functions, the short lifespan of PHHs, and a large variation in cellular functions among donor subjects, especially in metabolic enzyme activities.[7,8] To overcome the disadvantages of the 2D-PHHs, the 3D culture may be the best alternative model in pre-clinical drug discovery and screening. Spheroid and organoid are 3D cultures constructed by an aggregation of at least one cell type. They can resemble the in vivo model due to cell–cell and cell–extracellular matrix (ECM) interactions which promote physiological functions and represent pathological features depending on cell types.[9] While growing PHHs in a 3D coculture between PHHs and nonparenchymal liver cells (NPCs), the 3D-HPPs are able to detect 69% of all hepatotoxic compounds without producing any false positive results (100% specificity).[10] The coculture spheroids between PHHs and NPCs, including Kupffer cells (KCs), biliary cells (BCs), and hepatic stellate cells (HSCs), demonstrate phenotypically stable and retain morphology, viability, and hepatocyte-specific functions for long-term culture.[11] Nevertheless, 3D-PHHs have their own challenges such as the complicated culture techniques, the variation in growing protocols and excessive cost.[12] In fact, an interdonor variability has recently been observed in 3D-PHHs.[7]

Apart from PHH models, stem cell-derived hepatocyte-like cells and hepatoma cell lines (such as HepG2) are promising alternative cell sources for in vitro liver model because they are commercially available and easy to maintain.[4,5] The hepatocyte-like cells can be differentiated from pluripotent stem cells (iPSCs) and mesenchymal stem cells (MSCs) using transduction of transcription factors together with the treatment of growth factors and cytokines. However, the hepatic functions, such as drug metabolism capacity, of the 2D hepatocyte-like cells are known to be lower than those of the 2D-PHHs.[13,14] Therefore, the 3D hepatocyte-like cells have been developed in both monoculture and coculture with endothelial cells (ECs) to improve hepatocyte maturation. Although the expressions of the liver functions including albumin (ALB), hepatic transporters, and metabolic enzymes in the 3D hepatocyte-like cells have been observed to be higher than those in the 2D culture, their metabolic activities for U.S. FDA recommended drug have never been observed.[15–17]

2D HepG2 culture has currently been used as the in vitro liver model for screening drug-induced liver injury. Compared to PHHs, HepG2 cells exhibit poor expression and low activity of drug-metabolic enzymes which hinder the monitoring of metabolism-dependent toxicity.[18,19] 3D-HepG2 monoculture has been reported to improve hepatic functions in comparison to the conventional 2D-HepG2 culture.[20,21] The developed coculture system of 3D-HepG2-NIH/3T3 spheroids has been reported to enhance intrinsic secretion of albumin in long-term culture, but other liver functions including hepatic transporters and drug metabolism activities have not been entirely investigated.[22] Furthermore, for in vitro cancer model, 2D cultures using cancer cell lines have been a standard in vitro model for the current anticancer drug discovery research. 3D spheroids constructed from human cancer cells could be the versatile models for screening novel anticancer drugs because they represent both cellular heterogeneity and avascular tumor architecture, which promote chemoresistance, invasion, and migration in cancer. 3D-HepG2 cultures exhibit strong resistance to anticancer drugs[23] and the cocultures between HepG2 cells and HSC enhance the expression collagen type I (COL1) and matrix metallopeptidase 9 (MMP9) which act as a physical barrier and promote migration, respectively.[24]

HSCs play critical roles in both liver physiology and hepatocarcinogenesis. HSCs localize in the subendothelial space of Disse and interpose between liver sinusoidal endothelial cells and hepatocytes. They are usually accounted for 5%–10% of all liver-resident cells. In normal liver, quiescent HSCs are known as vitamin A-storing cells. During liver injury, HSCs are activated and transformed to myofibroblasts which are proliferative and responsible for collagen production.[25,26] Activated HSCs (aHSCs) support the reconstruction of liver structure and the improvement of liver function after liver injury by producing growth factors and ECM. However, excessive activation of HSC activation, inflammatory cytokines, and pro-angiogenic mediators can lead to the development of HCC.[27,28] Thus, to understand the interplay between hepatocytes and HSCs in normal liver as well as hepatoma cells and HSCs in HCC, the effects of HSCs on the coculture system must be comprehensively studied.

We hypothesized that the 3D construction of coculture between imHCs together with HSCs could enhance hepatic phenotypes and functions by increasing cell–cell interactions and recreate cell–cell junctions.[17] In addition, oxygen (O_2) gradient in the 3D spheroids may attribute to functions of hepatocytes in 3D model.[29,30] We also hypothesized that the 3D-HepG2-HSC coculture models could present HCC characteristics more than that of the 3D-HepG2 monoculture because the crosstalk between HepG2 and HSCs could increase liver cancer biomarkers relating to in vivo HCC as well as the reconstruction of biological barriers in the spheroids to resist anticancer drugs. Here, the mesenchymal stem cell derived-immortalized hepatocytes like cells (imHCs) established in the previous report[14] were fabricated both monoculture and coculture with HSCs using the ultralow attachment (ULA) method. HSCs ranging from 5% (Co5%), 10% (Co10%), and 15% (Co15%) were cocultured to study the interaction between imHCs and HSCs on hepatic maturation and functions. Similarly, HepG2 monoculture and HepG2 coculture with HSCs were developed and compared between mono- and coculture systems and between different cell type systems. Both mono (HepG2/imHCs) and coculture (HepG2/imHCs and HSCs) models were investigated on spheroid morphology, cell distribution, oxygen gradient, and functions. All native liver characters and liver cancer biomarkers were determined and monitored throughout the 3D model developing process. To fulfill the

D. Elson
Department of Surgery and Cancer
Imperial College London
South Kensington Campus
Exhibition Road, London SW7 2AZ, UK

A. E. Porter
Department of Materials and London Centre for Nanotechnology
Imperial College London
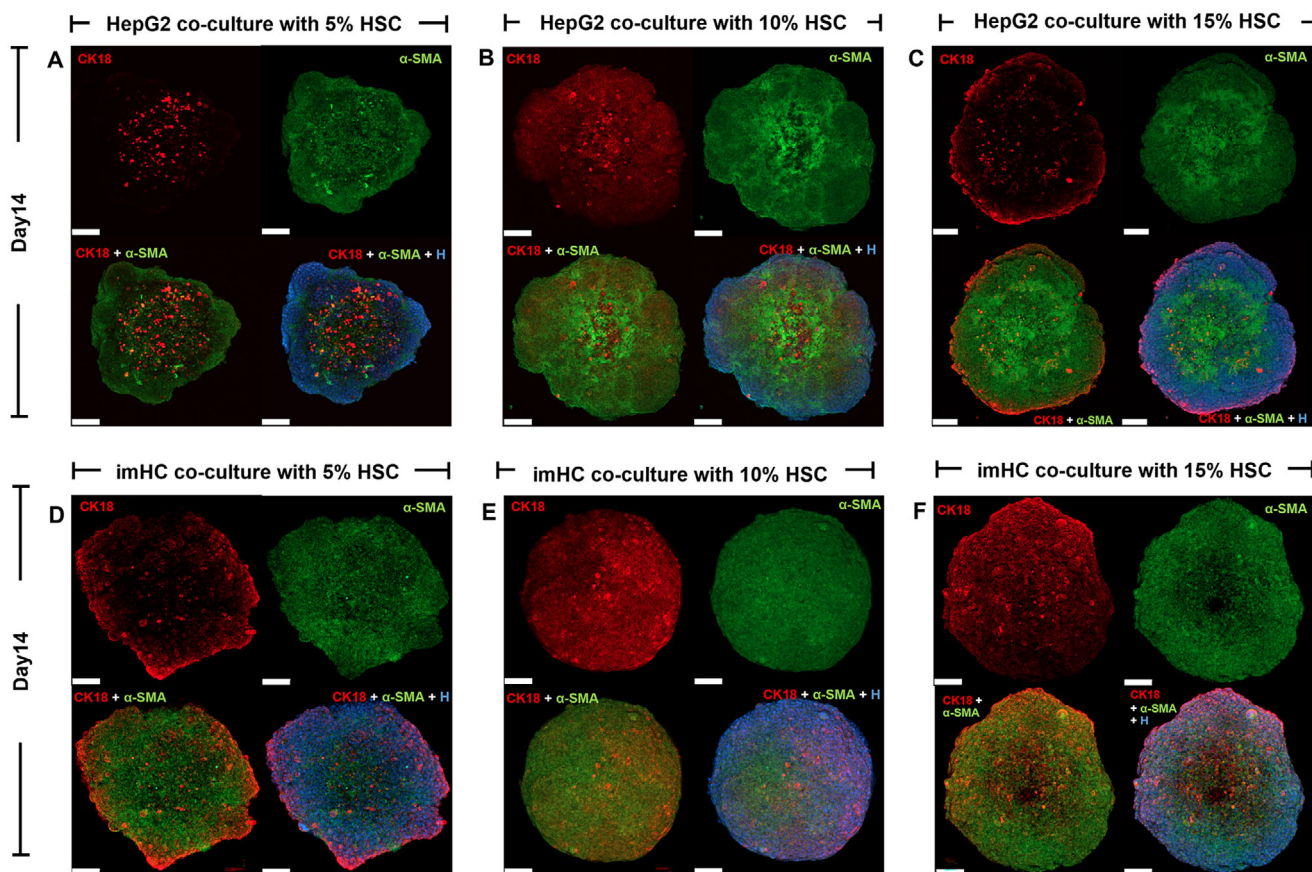Exhibition Road, London SW7 2AZ, UK

**ADVANCED
SCIENCE NEWS**

www.advancedsciencenews.com

**ADVANCED
THERAPEUTICS**

www.advtherap.com

Figure 1. Spheroids morphology and cell distribution: Confocal fluorescent images demonstrated morphology and cell distribution at day 14 of A–C) 3D-HepG2 and D–F) imHC coculture with 5%, 10%, and 15%HSCs at day 14. Nuclei (H; Hoechst 33342), Cytokeratin 18 (CK18; a hepatocyte biomarker), and α-smooth muscle actin (α-SMA; an aHSC biomarker), Scale bars are 100 µm.

hepatocyte function, formations of drug metabolites were measured. The developed 3D spheroids were finally used for the anticancer screening using doxorubicin (DOX) as a model drug .

2. Results and Discussion

2.1. Cell Distribution within 3D-Liver Spheroids, Size Distribution, and Morphology

Either imHCs or HepG2 were seeded into the 96-well ULA plates to develop the 3D-monoculture model. Coculture spheroids were fabricated by seeding 5% (Co5%), 10% (Co10%), and 15% (Co15%) of HSCs together with imHCs or HepG2 in the 96-well ULA plates. After seeding the cells in 96-well ULA plates for 48 h, the cells aggregated and formed spheroids. The distribution of HSC within the 3D coculture spheroids was observed from day 7 to day 14 by immunofluorescent technique. Alpha-smooth muscle actin (α-SMA) representing an aHSC biomarker was employed to identify HSCs in the 3D coculture systems.[31,32] HSCs spontaneously undergo an activation process during cultivation as they cannot be maintained quiescent phenotypes at in vitro condition.[32,33] Both imHC and HepG2 were determined using cytokeratin18 (CK18), a hepatocyte-specific biomarker.[14,34] The distribution of aHSC was homogeneously observed through-

out coculture of imHC/HepG2 spheroids from day 7 to day 14 (**Figure 1**A–F, Figures S1 and S2, Supporting Information).

The diameter (Feret's diameter) and sphericity index (SI) of the developed spheroids (**Figure 2**A–F) were measured to investigate the morphological changes during spheroid growth from day 7 to day 14. Spheroid diameters of each group were highly uniform (Figure 2A,B,D,E). The diameters of the developed spheroids both mono and cocultures increased in a time-dependent manner (Figure 2A,D). There was significant difference in diameters between monoculture and cocultures of both cell types, *$p < 0.05$, **$p < 0.005$, ***$p < 0.0005$, ****$p < 0.0001$, $n = 3$ (five spheroids each, total 15 spheroids, Figure 2A,D). Due to high proliferation rates of cancer cells,[33] 3D-HepG2 monoculture exhibited the largest size, 736.41 ± 57.03 µm compared with other types of spheroids at day 14 (Figure 2A). Sizes of 3D-HepG2 and 3D-imHC cocultures were remarkably smaller than that of the monocultures because the presence of aHSCs could increase the compactness and density of the spheroids.[35] Similarly, sizes of 3D-imHC coculture spheroids with 15%HSCs exhibited the smallest size among 3D-imHC spheroids (Figure 2D). SI is used to classify the spherical (SI $\geq$ 0.90) and nonspherical morphology of spheroids (SI < 0.90; irregular shape such as rod, ellipsoidal, 8-shaped, etc.).[36] At day 14, the SI values of both 3D-HepG2 and 3D-imHC spheroids were slightly decreased
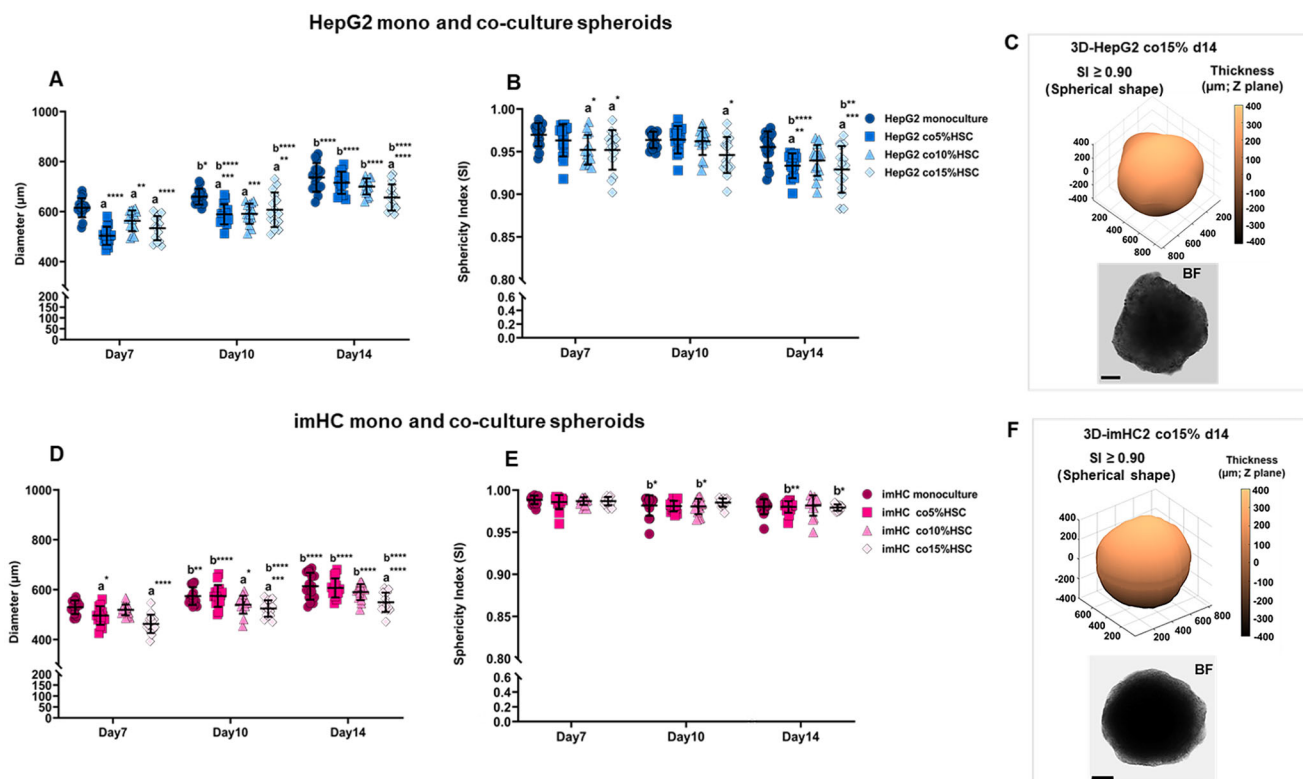
**ADVANCED
SCIENCE NEWS**

www.advancedsciencenews.com

**ADVANCED
THERAPEUTICS**

www.advtherap.com

Figure 2. Spheroids morphology and cell distribution: diameter (Feret's diameter; A, D) and sphericity index (SI; B, E) of the developed A,B) HepG2 and D,E) imHC mono and coculture spheroids were compared. The diameters of HepG2 and imHC monoculture models were larger than the coculture (5%, 10%, and 15%HSCs). Both mono and coculture of 3D-HepG2 and 3D-imHC demonstrated the largest size at day 14. Mean of SI of 3D-imHC and HepG2 mono and coculture spheroids was higher than 0.90 over 14 d. Mean ± s.d, two-way ANOVA, *$p < 0.05$, **$p < 0.005$, ***$p < 0.0005$, ****$p < 0.0001$, $n = 3$. C) The SI of two from 15 spheroids of 3D-HepG2 coculture with 15%HSCs at day 14 was lower than 0.9 (SI = 0.883 in B) defined as nonspherical shape. In contrast, the SI of 3D-imHC coculture with 15%HSCs at day 14 was higher than 0.9 defined as spherical shape (E-F). 3D-projection images of C) 3D-HepG2 and F) imHC coculture with 15%HSCs at day 14 were reconstructed by ReViSP.[36] BF = Bright field.

compared to day 7 (Figure 2B,C,E,F). The spheroids of imHC monoculture (SI = 0.954–0.994) and coculture models (SI = 0.950–0.993) were found in spherical shapes (SI ≥ 0.90) for 14 d whereas nonspherical shapes (SI = 0.883; irregular shapes) were also observed in some populations of the HepG2 coculture models with 15%HSCs at day 14 (Figure 2C) due to uncontrollable cell proliferation and disorganized growth of cancer cells. Spheroids with the irregular shape may impact on the penetration of drug substances resulting in large variability in in vitro assays.[36]

2.2. Protein Expression of Liver-Specific Biomarkers

As mentioned in the results of cell distribution part, the expression of CK18 was observed in both 3D-imHC and 3D-HepG2 spheroids (Figures S3 and S4, Supporting Information) indicating that imHC and HepG2 possessed the hepatocyte phenotype in the developed 3D structures. To completely resemble hepatocyte polarity and liver sinusoidal architecture, multidrug resistance protein 2 (MRP2, Figures S5 and S6, Supporting Information), cytokeratin 19 (CK19, Figures S7 and S8, Supporting Information), and zona occluden-1 (ZO-1; tight junctions [TJs], **Figure 3**) were employed to identify hepatic transporters, biliary

cells, and cell–cell junction, respectively.[12,37] The observation of TJ formation may help to indicate the structural polarity liver polarity in the developed 3D models. The structural polarity in normal liver, the bile canaliculi are functionally sealed by TJs. In contrast, TJ dysregulation has been observed in chronic liver disease and HCC.[38,45] The presence of ZO-1 (Figure 3) could indicate the liver sinusoidal architecture in both 3D-HepG2 and 3D-imHC spheroids.[38,46] However, the strong signal of the junction between imHC/HSCs and HepG2/HSCs was not observed in the coculture systems (Figure 3). At different culture periods, both developed 3D-HepG2 and 3D-imHC models expressed all biomarker proteins at day 7 and remained for 14 d (**Figure 4**; Figures S5 and S8, Supporting Information), but the different levels of protein expression depended on cell types, culture period, and ratio of coculture. The protein expression levels, MRP2 and CK19, were measured and compared by mean fluorescent intensity (MFI) between mono and coculture from day 7 to day 14 as seen in Figure 4.

MRP2, a canalicular efflux transporter, locates at the canalicular (apical) membrane of hepatocytes to transport drugs and drug metabolites from blood into bile.[38] Both HepG2 and imHC mono and coculture models expressed MRP2 from day 7 (Figures S5 and S6, Supporting Information). The highest MRP2 expression in 3D-HepG2 monoculture
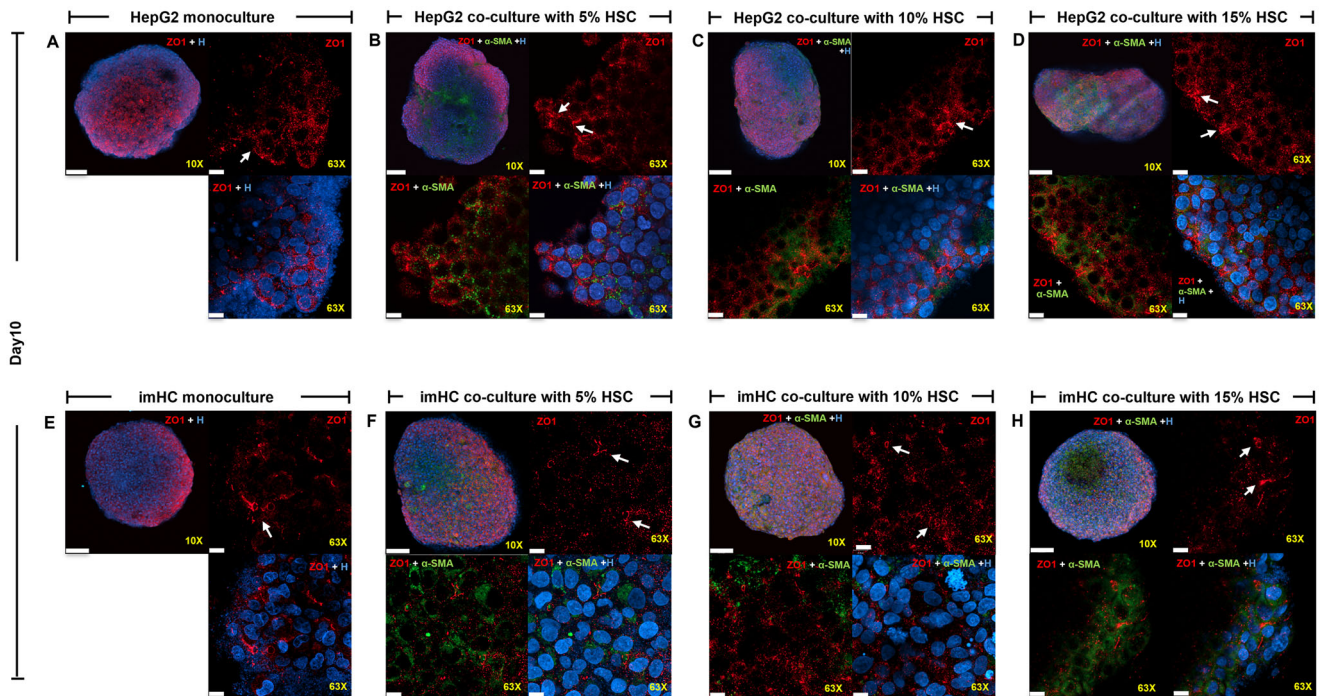
Figure 3. Tight junctions (TJs) in 3D liver spheroids: confocal fluorescent images demonstrated TJs using zona occludin1 (ZO1) at day 10 of A–D) 3D-HepG2 and E–H) imHC coculture with 5%, 10%, and 15%HSCs. Nuclei (H; Hoechst 33342), Zona Occludin1 (ZO-1; a hepatocyte biomarker), α-smooth muscle actin (α-SMA; an aHSC biomarker), Scale bars are 100 μm for 10× magnification and 10 μm for 63× magnification.
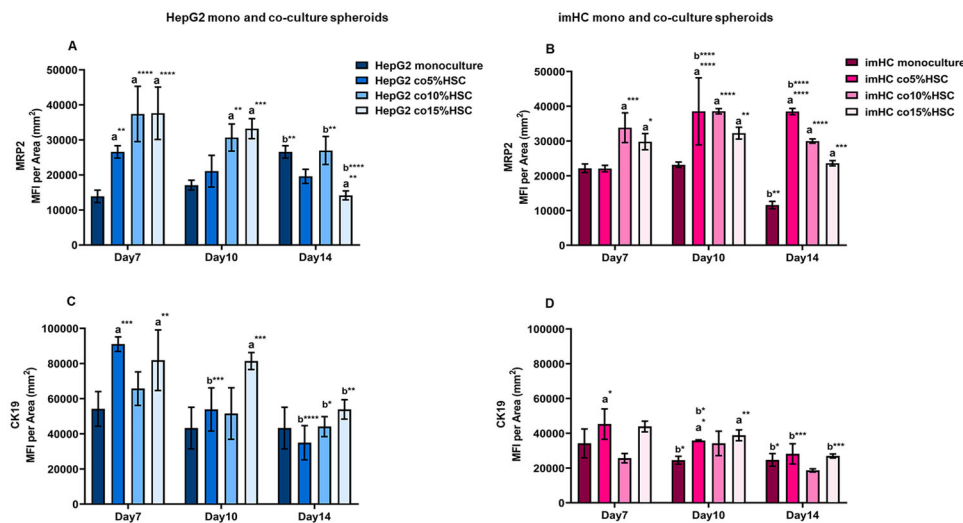

Figure 4. A,B) Expression of MRP2 and CK19 in 3D-liver models: mean fluorescent intensity per area (mm³) of MRP2 expressed in 3D-HepG2 and 3D-imHC models and C,D) expressions of CK19 biomarkers in 3D-HepG2 and 3D-imHC models; the results were compared between the mono and coculture models. HepG2 coculture with 15%HSCs and imHC coculture with 10%HSCs exhibited the highest levels of MRP2 expression at day 7 and day 10, respectively. In contrast, at day 7, HepG2/imHC coculture with 5%HSCs exhibited the highest levels of CK19. Mean ± s.d, two-way ANOVA, $*p < 0.05$, $**p < 0.005$, $***p < 0.005$, $****p < 0.0001$, $n = 3$.

spheroid was observed at day 14, while, the level of MRP2 expression in 3D-HepG2 coculture models was at the highest at day 7, and the expression was significantly reduced over the time of observation comparing to 3D-HepG2 monoculture model (**Figure** 4A). Recent reports indicated that the high expression of MRP2 relates to chemoresistance in HCC patients resulting in

low efficacy of HCC treatment.[39,40] Therefore, the current developed 3D-HepG2 coculture model may be useful for studying the mechanism of drug resistance and predicting efficacy of novel anticancer drugs for HCC treatment. The highest MRP2 expression in 3D-imHC mono and coculture models was observed at day 10 (Figure 4B). The imHCs with 10%HSCs considerably exhibited
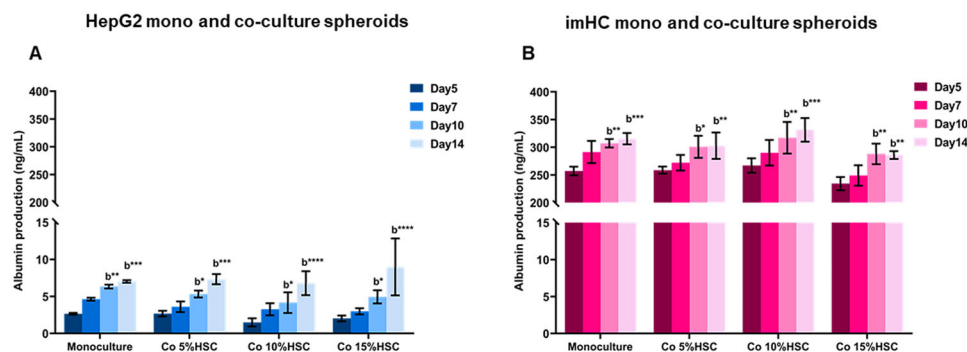
Figure 5. Albumin production in 3D-liver models using ELISA: The cumulative production of ALB in A) 3D-HepG2 and B) 3D-imHC models, the results were compared between mono and coculture models at day 5 to day 14. The ALB productions of 3D models were continuously increased from day 5 to day 14 in both types. ALB production in monoculture of 3D-HepG2 and 3D-imHC models was not significantly different from the coculture models. Mean ± s.d, two-way ANOVA, $*p < 0.05$, $**p < 0.005$, $***p < 0.0005$, $****p < 0.0001$, $n = 3$.

higher level of MRP2 expression than that of monoculture model from day 7 to day 14 (Figure 4B). In normal liver, hepatobiliary elimination is a major clearance pathway that dictates drug pharmacokinetics. MRP2 plays a vital role in to efflux not only anionic drugs but also conjugated-drug metabolites including conjugated bilirubin from hepatocytes into canaliculi. Thus, the high expression of MRP2 may affect the clearance of MRP2 drug substrates. While the inhibition of MRP2 in the hepatocytes can causes toxic accumulation of drugs and conjugated bilirubin.[41] Thus, 3D-imHC spheroids might be further used to predict substrates or inhibitors mediated MRP2.

To further confirm formation of bile duct, CK19, a biomarker of bile duct epithelial cells, were observed in 3D-liver models.[12] (Figures S7 and S8, Supporting Information). All models expressed CK19 at day 7, and the expression levels decreased toward culture period of 14 d (Figure 4C,D). Results demonstrated the highest expression of CK19, at day 7, in 3D-HepG2 (mono and co5-15%). The coculture models of 5% and 15% significantly exhibited higher levels of CK19 than the 3D-HepG2 monoculture model (Figure 4C,D). While the level of CK19 in 3D-imHC (mono and co5% and co15%) showed the highest expression at day 7 and at day 10 in 3D-imHC with 10%HSCs. Both MRP2 and CK19 expressions revealed hepatocyte polarity phenotypes and the structure of bile canaliculi within the currently developed spheroid models.[12,37,38]

CK19 is also acknowledged as a marker of progenitor cells and tumor stem cells. CK19-positive area in HCC is associated with poor tumor differentiation, tumor recurrence and metastasis, as well as poor prognosis.[42] CK19 has recently become an immunohistological marker for poor prognosis in HCC patients.[43] High expression of CK19 in 3D-HepG2 coculture spheroids might be reemerged due to the HepG2-HSC interaction. Therefore, the developed 3D-HepG2 coculture model may be useful for investigating the role of CK19 in tumor and finding new target molecules against CK19-positive HCC.[44]

ALB was used to investigate the liver function of all developed spheroid models.[17,23,45] To examine the liver function at different stages of spheroid growth, the supernatants were collected from day 5 (early-stage spheroids) to day 14 (late-stage spheroids).[23] The ALB production of 3D models was detected from day 5 of the culture and it continued to increase, significantly, for 9 d in both

types of cell models (**Figure 5**A,B). Unlike the saturation of ALB production in 2D culture models,[15] the ALB level of 3D models increased in time-dependent manner (Figure 5A,B). The secreted ALB of 3D spheroids at day 10 and day 14 was significantly higher than day 5. As a normal liver routinely produces ALB in vivo, these results indicated that both 3D-imHC mono and coculture spheroids remained functionally active. The ALB produced by 3D-imHC coculture model with 10%HSCs was 338.17 ± 13.19 ng mL^{-1} at day 14, and it was slightly higher than the ALB produced by the 3D monoculture spheroids, 315.49 ± 10.30 ng mL^{-1}. While the ALB was also produced in both 3D-HepG2 monoculture and coculture models. The ALB produced by 3D-HepG2 monoculture model was slightly higher than the ALB produced by the 3D-HepG2 coculture spheroids during day 5 to day 10. Thus, the coculture with HSCs did not significantly impact on the ALB production of both imHC and HepG2 spheroid models.

2.3. Comparison Phase I and Phase II Expressions between Monoculture and Coculture Models between Monoculture and Coculture Models with Their O$_2$ Mapping

According to the previous results, the coculture spheroid model of imHCs and 10%HSCs demonstrated the higher expression levels of ALB and MRP2 than that of the monoculture spheroid models. Therefore, the coculture models of 10%HSCs with imHCs/HepG2 cells were selected for further investigation and compared the expression of phase I (Cytochrome P450; CYP450) and phase II (Uridine 5′-diphospho-glucuronosyltransferase; UGT) metabolic enzymes with the monoculture models. We investigated all basal CYP450 expressions, following the U.S. FDA guideline for evaluating the drug–drug interactions (DDI)[6] (**Figure 6**A–G). The expression levels of CYP450 expressions in both developed 3D-HepG2 and imHC-spheroid models were found at the highest levels at day 10, except the expression levels of CYP1A2 where the maximum expression was detected at day7 (Figure 6A).

Similarly, the previous study revealed that HepG2 spheroids could increase liver-specific activities between day 9 and 18 compared to early stage (days 3–5).[23] 3D spheroids could present O$_2$ gradient to mimic zonation of in vivo liver lobule which

**ADVANCED
SCIENCE NEWS**

www.advancedsciencenews.com
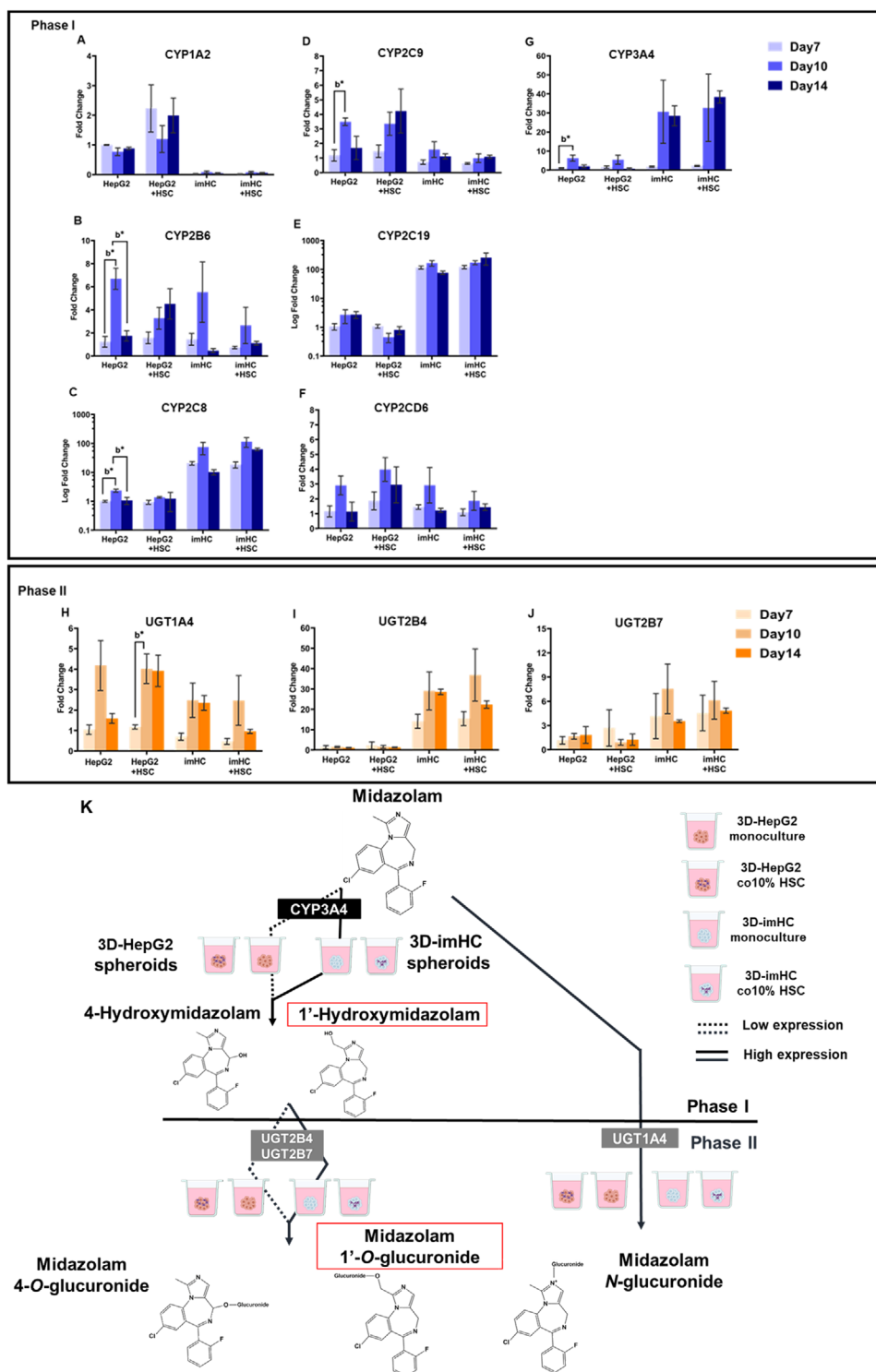
**ADVANCED
THERAPEUTICS**

www.advtherap.com

Figure 6. Quantitative reverse transcription-polymerase chain reaction (qRT-PCR) analysis of A–G) phase I and H–J) phase II metabolic Cytochrome P450 enzyme (CYP450) expression in 3D-imHC and 3D-HepG2 both mono and coculture models. The fold changes in gene expression levels of 3D spheroids at day 7, day 10, and day 14 were compared to 3D-HepG2 day 7 ($n = 3$; day 7 and day 14, $n = 4$; day 10). Mean ± SEM, two-way ANOVA, $*p < 0.05$. The proposed metabolism pathway of midazolam through phase I (1'-Hydroxymidazolam) and phase II (Midazolam 1'-O-glucuronide) enzymes monitored over 72 h.

**ADVANCED
SCIENCE NEWS**

www.advancedsciencenews.com

**ADVANCED
THERAPEUTICS**

www.advtherap.com

could involve in the expression of metabolic enzymes in the liver. Recently, the zone-dependent differences in the expression of metabolic enzymes have been reported.[47,48] In vivo sinusoidal oxygen decreases from 60 to 65 mm Hg (8%–9% O_2) at the portal layers to about 30–35 mmHg (3%–4% O_2) at pericentral layers.[49] In addition, oxygen (O_2) gradient in the 3D spheroids attributes to zonation in liver lobule, where the perivenous zone was usually detected at the center area (quiescent viable zone) and the gradient incrementation of O_2 in periportal zone was observed toward the spheroid surface (proliferating zone). Here, the gradient levels of O_2 in both monoculture and coculture with 10%HSCs were indirectly evaluated using Image-iT Green Hypoxia Reagent. Both 3D-HepG2 and 3D-imHC monoculture and coculture spheroids demonstrated the positive-O_2 gradient between pericenter zone (low $O_2 < 5\%$) and peripheral zone (Figure S9, Supporting Information). Hypoxia was observed at the core of 3D-HepG2 and 3D-imHC spheroid models. Due to limitation of oxygen and nutrition diffusion, 3D-spheroids become hypoxic at the center which is frequently observed in the large diameter spheroids (starting from about 500 µm).[50,51] In addition, the shape[36] and the tightness of cellular interactions[52] within the spheroids have profound effect on the limitations of chemical substance diffusion. Therefore, the deliberate control of these parameters is necessary to obtain reproducible spheroids. Although the effect of hypoxia on metabolic enzyme expressions in 2D liver cells has been reported,[53] the significant alteration of both metabolic enzyme expressions and activities in 3D liver spheroids needs to be, completely, examined. Other reports showed that the activity of CYP2D6 and CYP2C19 were elevated in hypoxic spheroids due to an increased production of nicotinamide adenine dinucleotide phosphate oxidase (NAD(P)H) through hypoxia-induced glycolysis.[54]

3D-imHC mono and coculture models expressed high levels of CYP2C8, CYP2C19, and CYP3A4. While the outstanding expressions of CYP1A2, CYP2C9, CYP2B6, and CYP2D6 were observed in 3D-HepG2 mono and coculture models. In addition, we also investigated UGT-phase II metabolic enzymes (Figure 6H–J) including UGT1A4, UGT2B4, and UGT2B7. At day 10, the highest levels of UGT-phase II enzymes were detected in 3D-imHC models. In contrast, 3D-HepG2 monoculture and coculture models remarkably expressed UGT1A4. However, we found that the presence of HSCs did not significantly increase both phase I and phase II activities, compared with the developed monoculture models.

Thus, at day 10 after seeding, the spheroids were collected and incubated with probe CYP450 substrates to investigate the amount of drug metabolites via CYP3A4, CYP2C9, and CYP2D6. These CYP450s were selected because CYP3A4 and CYP2C9 isoforms have been the most expressed in CYP3A and CYP2C subfamilies. Approximately 40% of pharmaceutical substances have been metabolized through CYP3A4. CYP2D6 has been exclusively focused on the development of novel anticancer drugs due to its role in the production of active metabolites of some anticancer drugs (e.g., tamoxifen).[55] In addition, the expressions of UGT1A4, UGT2B4 and UGT2B7 have been related to the formation of glucuronide-conjugated midazolam.[56,57]

The drug metabolites of three standard drugs, dextromethorphan (CYP2D6), tolbutamide (CYP2C9), and midazolam (CYP3A4), were observed at low levels after 4 h of monitoring period and the levels increased toward 72 h. The differences in the quantity of drug metabolites were depending on incubation period and spheroid types (**Table 1**). In general, the amount of drug metabolites (dextrorphan, hydroxytolbutamide, and 1′-hydroxymidazolam) transformed via the developed 3D coculture models were slightly higher than the 3D-monoculture models, except hydroxytolbutamide that was higher in 3D-HepG2 monoculture (Table 1).

Even though, CYP2D6 and CYP2C9 expressions by 3D-HepG2 spheroids were not found to be much different from 3D-imHC spheroids, the amount of dextrorphan and hydroxytolbutamide in the supernatants of 3D-imHC spheroids was significantly higher than that in 3D-HepG2 spheroids. In addition, hydroxytolbutamide could not be detected following 4 h incubation period (Table 1) because tolbutamide hydroxylase might have been at low activity, compared to midazolam 1′-hydroxylase and dextromethorphan-O-demethylase. To fully address the results, the kinetic parameters including affinity (K_m) and maximum rate of a metabolic enzyme (V_{max}) of enzymes in each cell type must be further investigated. These parameters should also be taken into consideration since the metabolic gene expressions and CYP450 activities were different among in vitro hepatocyte models.[58]

Due to the expression of CYP3A4 and the high amount of 1′ hydroxymidazolam in supernatants of 3D-imHC coculture spheroids (Figure 6G), midazolam 1′-O-glucuronide was detected in 3D-imHC coculture models following 72 h incubation period, although, the detected level was found to be lower than 2.5×10^{-9} M (LLOQ, Table 1). This is the first report to detect the glucuronide-conjugated midazolam using 3D spheroids fabricated by hepatocyte-like cells. These results allowed us to propose a metabolism pathway of midazolam by the developed 3D models (Figure 6K). In this study, we only detected level of 1′-hydroxymidazolam in phase I and midazolam 1′-O-glucuronide in phase II, therefore, we could not identify all metabolites of midazolam through the proposed metabolic pathway by the developed 3D models. The further measurement of the levels of 4-O-glucuronide and N-glucuronide are needed. In comparison, the developed 3D liver spheroids could improve CYP2D6 and CYP2C9 activities compared to the previous developed 2D-PHHs (**Table 2**).[59,60] 3D-HepG2 models might be further investigated to turn prodrug of novel anticancer drugs for HCC treatment into an active form via CYP2D6. Furthermore, the developed 3D-imHC construction could provide a routine evaluation of the full length of CYP450 expressions (phase I and II) together with detectable level of drug metabolites.

2.4. Protein Expression of HCC-Specific Biomarkers

HCC specific biomarkers including COL1, alpha-fetoprotein (AFP), interleukin-6 (IL-6), and vascular endothelial growth factor (VEGF) are used to identify HCC phenotypes. In normal liver, laminins, type IV collagen, and a mixture of proteoglycans are scattered within the hepatic ECM. While HCC was developing in chronically damaged liver tissue, COL1 produced from aHSCs had been found to be abundant in fibrotic liver.[24,25] Both developed 3D-HepG2 and 3D-imHC spheroid models expressed COL1 at day 7 and remained for 14 d (Figures S10 and S11, Supporting Information). The COL1 expression levels in

Table 1. Assessment of drug metabolites: dextrorphan, 1′-hydroxymidazolam, and hydroxytolbutamide were detected in supernatant of 3D-imHC and 3D-HepG2 spheroids via CYP2D6, CYP3A4, and CYP2C9 measured by LC-MS/MS.

Time	3D-HepG2 monoculture	3D-HepG2 co10%	3D-imHC monoculture	3D-imHC co10%
CYP2D6: Dextrorphan (pmol/10^6 cells)				
4 h	0.82 ± 0.36	0.79 ± 0.26	1.06 ± 0.07	2.38 ± 0.29
24 h	1.73 ± 0.23	2.38 ± 0.27	3.27 ± 0.57	7.24 ± 0.52
48 h	2.77 ± 0.46	3.43 ± 0.32	9.15 ± 1.72	18.54 ± 3.38
72 h	4.69 ± 1.13	5.34 ± 0.24	27.63 ± 6.31	33.80 ± 5.58
CYP2C9: Hydroxytolbutamide (pmol/10^6 cells)				
4 h	Not detected	Not detected	Not detected	Not detected
24 h	<LLOQ*	<LLOQ*	2.99 ± 1.26	3.12 ± 0.99
48 h	<LLOQ*	<LLOQ*	7.10 ± 1.65	11.40 ± 2.39
72 h	5.68 ± 1.14	4.81 ± 0.95	29.07 ± 5.74	37.19 ± 7.99
CYP3A4: 1′-Hydroxymidazolam (pmol/10^6 cells)				
4 h	<LLOQ*	<LLOQ*	0.88 ± 0.16	1.54 ± 0.15
24 h	0.53 ± 0.02	0.64 ± 0.12	2.62 ± 0.57	4.90 ± 0.99
48 h	0.69 ± 0.05	0.83 ± 0.08	7.21 ± 1.84	11.10 ± 1.16
72 h	1.16 ± 0.24	1.24 ± 0.12	21.84 ± 0.22	25.10 ± 3.47
UGT2B4 and UGT 2B7: Midazolam 1′-O-glucuronide (pmol/10^6 cells)				
4 h	Not detected	Not detected	Not detected	Not detected
24 h	Not detected	Not detected	Not detected	Not detected
48 h	Not detected	Not detected	Not detected	<LLOQ*
72 h	Not detected	Not detected	Not detected	<LLOQ*

Noted: The probe substrates to determine activities of phase I; CYP2D6, CYP2C9, and CYP3A4, and phase II; UGT2B4 and UGT2B7 were dextromethorphan, tolbutamide, and midazolam, respectively. *LLOQ of hydroxytolbutamide and Midazolam 1′-O-glucuronide were 2.5×10^{-9} M. Mean $\pm$ s.d, $n = 3$

Table 2. Detection of drug metabolites in in vitro liver models.

Metabolites	This study	Reported data		
		2D-PHHs[59]	2D-sandwich PHHs[7]	3D-PHHs[59,60]
CYP 2C9: Hydroxytolbutamide	Detected (>1 ng mL^{-1})	BDL (<1 ng mL^{-1})	Detected	Detected
CYP 2D6: Dextrorphan	Detected (>1 ng mL^{-1})	BDL (<1 ng mL^{-1})	Detected	Detected
CYP3A4: 1′Hydroxymidazolam	Detected	Detected	Detected	Detected
UGT2B4 and UGT 2B7 : Midazolam 1′-O-glucuronide	Detected	(Detected in liver microsomes)[53]		Detected

Note: The data of PHH models were obtained from other publications. The amount of drug metabolites was observed at day 10 after incubation CYP450 probes.

the 3D-HepG2 coculture models were significantly higher than the 3D-HepG2 monoculture model (**Figure 7**A,B,E,F). Between 5%, 10%, and 15% of HSC coculture model, the 5% HSC coculture model expressed COL1 at the lower levels than the 10% and 15% HSC coculture models. The COL1 expression in the 3D-imHC monoculture spheroid was found at the lower levels than that in 3D-imHC coculture models on day 7 to day 14 (Figure 7; Figures S10 and S11, Supporting Information). The developed 3D-imHC coculture models significantly increased level of COL1, compared with 3D-imHC monoculture model (Figure 7B–D). The high expressions of COL1 in 3D-imHC coculture models reached the maximum at day10, and the COL1 was observed at the core of the spheroids (Figure 7C) from day 7 of culture period. In contrast, the COL1 in 3D-HepG2 coculture models

homogeneously distributed throughout the spheroids indicating the difference in cell function of HepG2 and imHC. In comparison to the monoculture models, the presence of HSC together with HepG2 and imHC in 3D spheroid models could increase the COL1 production up to three times of the monoculture models.

Based on the observation that COL1 expression in the 3D-HepG2-HSCs (10%) coculture model was at the highest level on day 10 (Figure 7A). We, then, selected 10%HSCs-HepG2 coculture model to determine the amount of circulating HCC biomarkers including AFP, IL-6, and VEGF. Supernatants of 3D-HepG2 and 3D-imHC mono and coculture models were investigated from day 5 to day 14. AFP is a diagnostic biomarker for HCC. It has been well established that the persistent and elevated
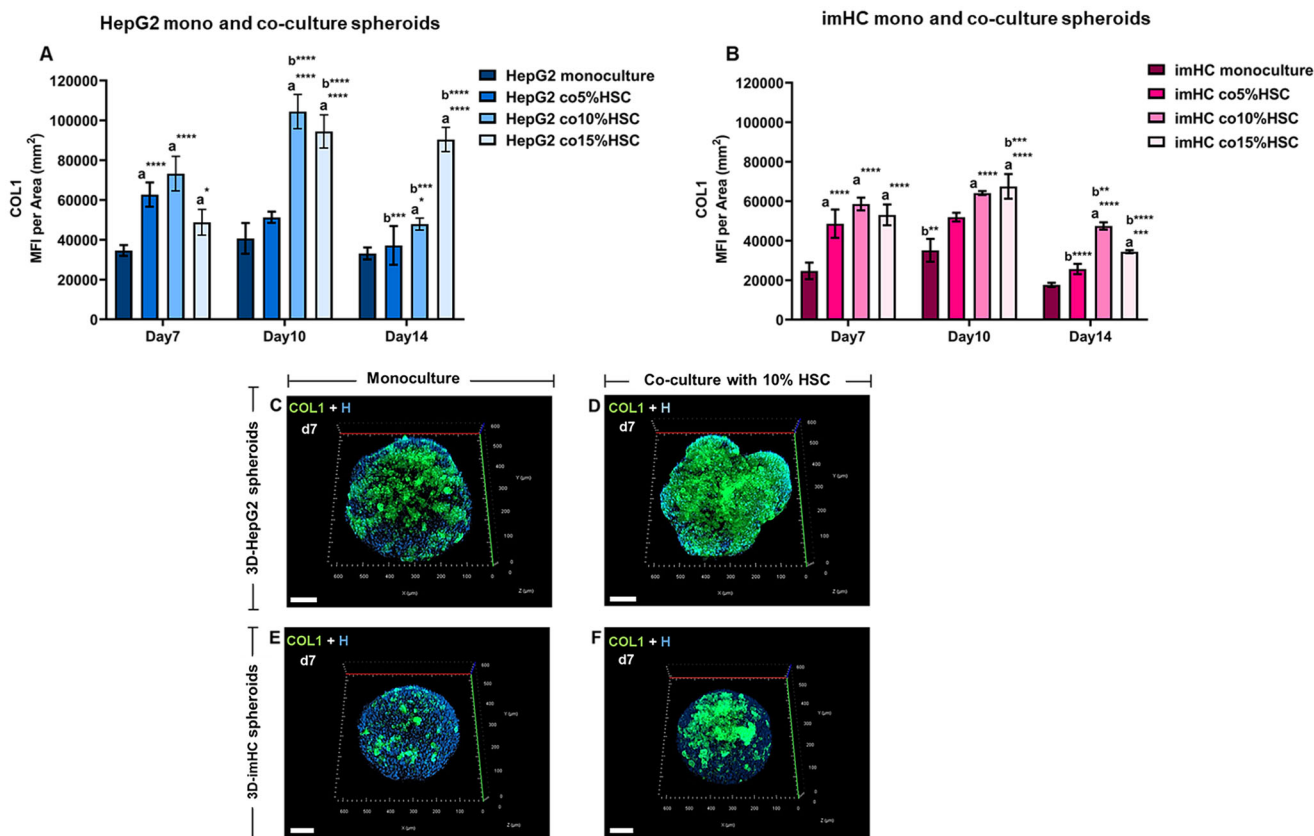
Figure 7. Expression of COL1 in 3D-liver models: mean fluorescent intensity per area (mm^3) of COL1 expressions in A) 3D-HepG2 spheroids and B) 3D-imHC spheroids were compared between mono and coculture models. HepG2 coculture with 10%HSCs and imHC coculture with 15%HSCs exhibited the highest level of COL1 expression at day 10. Mean ± s.d, two-way ANOVA, *$p < 0.05$, **$p < 0.005$, ****$p < 0.0001$, $n = 3$. 3D-confocal fluorescent images compared the distribution of COL1 in C,D) 3D-HepG2 and E,F) 3D-imHC at 7 day between mono and coculture with 10%HSCs. Nuclei (H; Hoechst 33342), Collagen type 1 (COL1; an aHSC biomarker), Scale bars are 100 μm.

AFP level (>20 ng mL^{-1}) is a risk factor for HCC development and can be used to define at-risk populations.[43] The amount of AFP was highest at day 7 in 3D-HepG2 mono and coculture models (**Figure 8**A,B). The AFP secretion of the 3D-HepG2 monoculture model, 138.54 ± 10.37 ng mL^{-1}, was slightly higher than the 3D-HepG2 coculture with 10%HSCs model, 138.12 ± 9.65 ng mL^{-1} (Figure 8A). Overall, similar levels of AFP were detected in supernatant of 3D-imHC models (Figure 8B). At day 7, the 3D-imHC monoculture model exhibited the highest amount of AFP, 135.79 ± 9.38 ng mL^{-1}, whereas the 3D-imHC coculture model showed the highest AFP secretion, 137.95 ± 9.35 ng mL^{-1}, at day 10 (Figure 8B). Unlike PHHs, iPSCs or MSCs derived imHCs consistently express AFP as a fetal hepatic marker in 3D models.[61,62] Thus, several studies considered the ratio between ALB and AFP (ALB/AFP) whether they increased over time to try to normalize the presence of AFP.[16,17,61] Our results found that the level of AFP in 3D-imHC model decreased from day 10 to day 14, while the ALB production continuously increased (Figure S12, Supporting information), suggesting an improvement in hepatocyte maturation within the model. The ALB/AFP of 3D-imHC monoculture was also increased significantly from day 10 to day 14. While the significant level of ALB/AFP was observed only at day 14 in 3D-imHC coculture models (Figure S12, Supporting Information).

VEGF is a major cytokine to promote angiogenesis in solid tumors. Hypervascularity and marked vascular abnormalities are one of hallmarks which are observed in HCC tumors.[63,64] VEGF concentrations in 3D-HepG2 and 3D-imHC spheroids were increased in time-dependent manner. Both mono and coculture of 3D-HepG2 spheroids demonstrated high level of VEGF, indicating the HCC phenotype (Figure 8C,D). The 3D-HepG2 monoculture model, 668.10 ± 27.76 pg mL^{-1}, exhibited slightly higher than the 3D-HepG2 coculture with 10%HSCs model, 549.84 ± 75.46 pg mL^{-1} (Figure 8C). As previously discussed, HCC is a prototypical inflammation-associated cancer. IL-6 has been observed with high levels in non-proliferation class of HCC.[64,65] In addition, IL-6 with cutoff 12 pg mL^{-1} could be considered a promising tumor marker together with AFP for HCC.[66] High expression of pro-inflammatory cytokine, IL-6, was only observed in the coculture of 3D-models. The highest amount of IL-6 was detected in the 3D-HepG2 coculture model at day 7, 24.74 ± 9.37 pg mL^{-1}, then, IL-6 secretion rapidly decreased from day 10 to day 14 (Figure 8E,F). Interestingly, at day 5, secreted IL-6 in the 3D-imHC coculture model was also high, 23.27 ± 1.19 pg mL^{-1}. The results suggested that HSCs could promote HCC progression including cytokine secretion and pro-tumorigenic ECM components. Thus, the coculture models fabricated by HepG2 and HSCs might be the potential model for investigating the
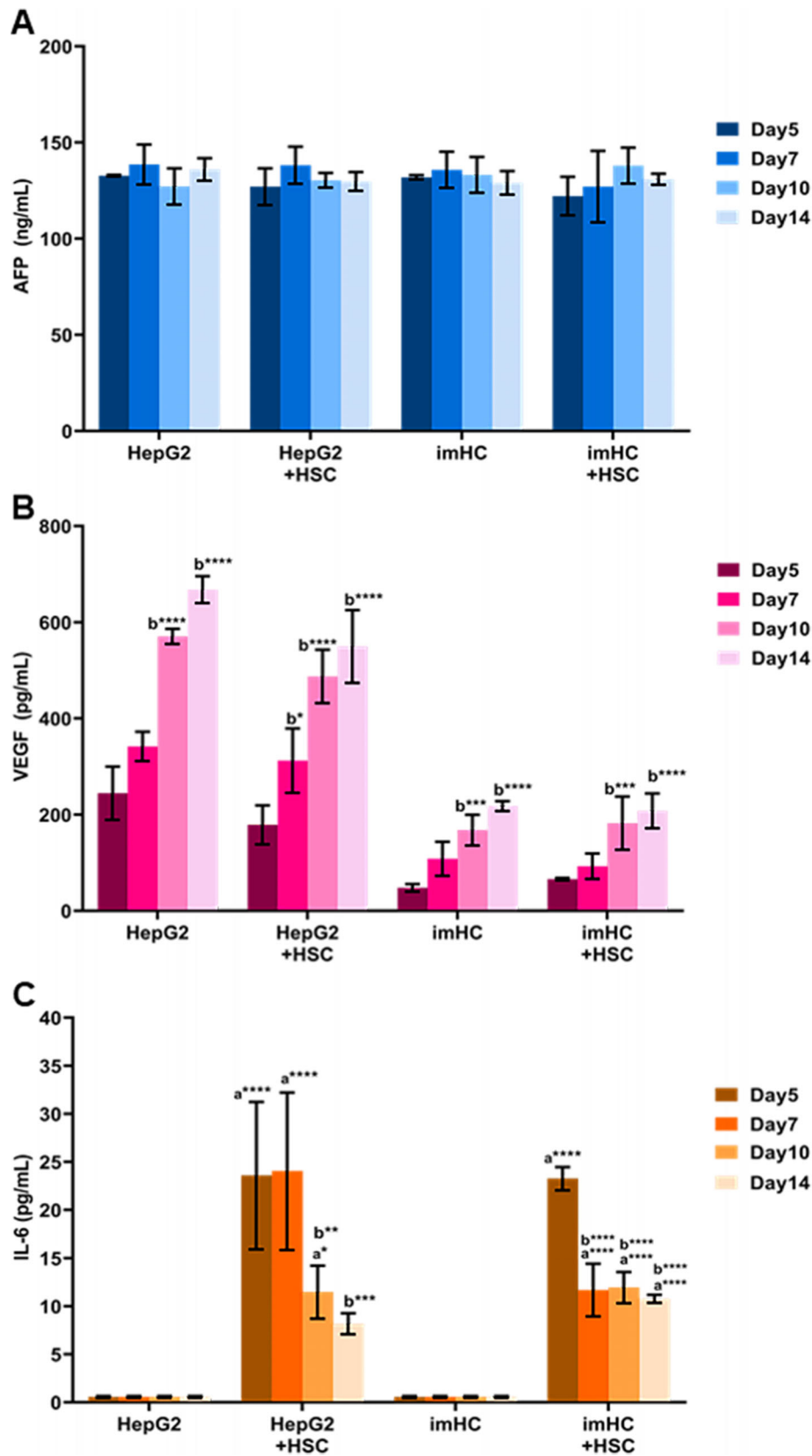
ADVANCED
SCIENCE NEWS

www.advancedsciencenews.com

**ADVANCED
THERAPEUTICS**

www.advtherap.com

Figure 8. The quantification of HCC biomarkers: A) AFP, B) VEGF, and C) IL-6 in developed 3D-HepG2 and 3D-imHC models for 14 d. All biomarkers were compared between day 5 and day 14. Mean ± s.d, two-way ANOVA, *$p < 0.05$, **$p < 0.005$, ****$p < 0.0001$, $n = 3$.

**ADVANCED
SCIENCE NEWS**

www.advancedsciencenews.com

**ADVANCED
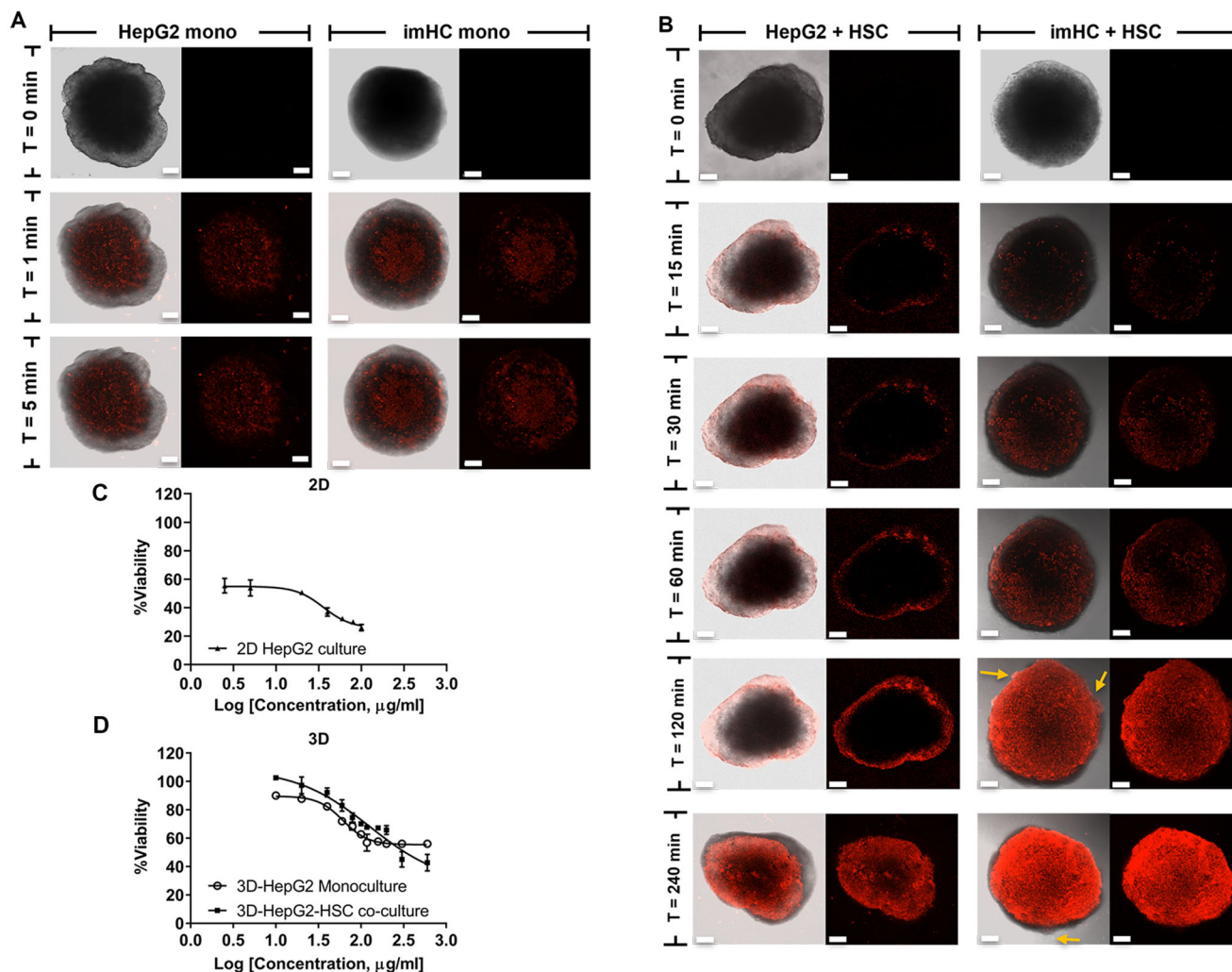THERAPEUTICS**

www.advtherap.com

Figure 9. Drug penetration study in 3D-liver models: Confocal fluorescent images demonstrated the penetration of DOX (red) into A) 3D-HepG2 and 3D-imHC monoculture and B) 3D-HepG2 and 3D-imHC coculture spheroids at time $T = 0$ to $T = 240$ min (4 h). Yellow arrow presented the detached cells of 3D-imHC coculture model at $T = 120$ min (2 h). Scale bars represent 100 μm. The inhibitory effect of DOX in C) 2D-HepG2 against monoculture model, D) 3D-HepG2 monoculture and 3D-HepG2-10%HSC coculture models.

underlying molecular mechanisms which relate to tumor microenvironment in anticancer drug development and could be used as in vitro model to find new therapeutic drugs which target to IL-6.[67]

2.5. Drug Penetration Study of Doxorubicin into 3D-Liver Spheroids

The complicity of coculture models was tested for their biological and physical barriers against drug penetration. Doxorubicin (DOX) was used as a model of anticancer drug. Comparing to the coculture, less barriers were observed in HepG2 and imHC monoculture spheroids as DOX could reach the internal core of the monoculture spheroids within 1 min following the addition (**Figure 9**A) highlighted an important role of extracellular matrix within solid tumor. In coculture models with 10%HSCs, DOX took up to 120 min (2 h) to reach the internal core of

the imHC spheroids and the cells started to detach from the spheroids (Figure 9B). While the penetration of DOX into the core of 3D-HepG2 coculture spheroids was detected at 240 min (4 h). Inhibitory effects of DOX against the 2D-HepG2 monoculture and 3D-HepG2 mono- and coculture were also investigated (Figure 9C,D). The 50% inhibition concentrations (IC_{50}) of DOX in 2D-HepG2 monoculture, 3D-HepG2 monoculture, and 3D-HepG2 coculture models were 35.88 ± 1.67, 61.40 ± 0.41, and 127.20 ± 6.27 μg mL^{-1}, respectively. In 3D-HepG2 monoculture and coculture models, the concentrations of DOX had to be increased up to two and three times of its concentration used in the 2D-HepG2 in order to initiate 50% inhibitory effect highlighted the poor representation of current 2D models. These results indicated that the 3D coculture model of HepG2 provided biological barriers observed in solid tumor challenging drug penetration. The accumulation of COL1 within the spheroids could increase spheroid compactness and acted as the addition biological barrier in solid tumors. The increase in ECM due to the crosstalk
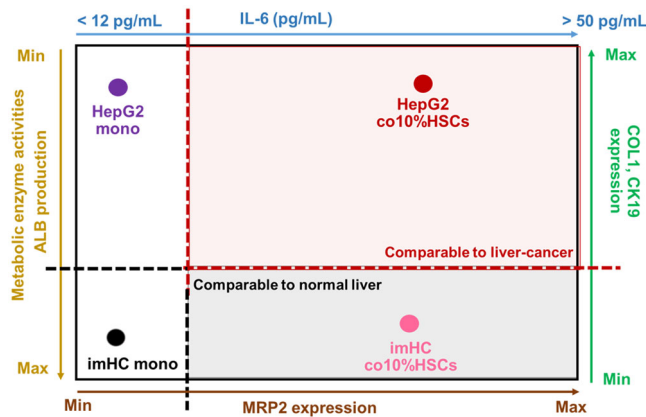
2200169 (12 of 16)

**ADVANCED
SCIENCE NEWS**

www.advancedsciencenews.com

**ADVANCED
THERAPEUTICS**

www.advtherap.com

Figure 10. Diagram illustrated characteristics of the novel developed spheroid models using ULA technique and this could be proposed into four categories: HepG2 monoculture (HepG2 mono), HepG2-HSC coculture (HepG2 co10%HSCs), imHC monoculture (imHC mono), and imHC-HSC coculture models (imHC co10%HSCs), respectively.

between hepatoma cells and HSCs in the coculture model could be significantly resilient to anticancer drugs.[24,68] Thus, the developed 3D-HepG2 coculture model might be promising as in vitro models for investigating novel anticancer drugs.

3. Conclusion

In this work, we have successfully developed both 3D monoculture and coculture models from imHCs, HepG2, and HSCs. The 3D spheroids were classified into four categories (**Figure 10**) using both normal liver biomarkers and liver cancer biomarkers. The 3D-imHC coculture model exhibited characteristics closed to in vivo normal liver and could be suitable for drug metabolism studies. However, the coculture model of imHC also expressed high level of IL-6 which relates to the interaction between imHCs and HSCs. Thus, the 3D-imHC coculture model is currently under investigation further for molecular alterations relating to early stage hepatocarcinogenesis. For the 3D constructed HepG2 models, the 3D-HepG2 coculture model could be useful for anticancer drug screening to find the novel targets (IL-6, COL1, and CK19), and studying drug resistance mechanism which mimicked in vivo HCC. Finally, the 3D-HepG2 monoculture models developed in this work were also employed as a control for validation of 3D-manupulation process. In conclusion, the presence of HSCs in 3D imHC coculture models could help to promote liver sinusoidal structure development (MRP2, CK19, and ZO1) and enhance the activity of CYP3A4 and CYP2D6. Although HSC could not improve hepatocyte functions of HepG2 coculture model, interestingly, the crosstalk between HSC and HepG2 significantly accelerated HCC phenotypes associating with HCC progression and chemoresistance.

4. Experimental Section

Cell Culture and Spheroid Construction: HepG2, imHCs, and HSCs were cultivated in a complete medium (GE Healthcare HyClone, USA) containing Dulbecco's modified eagle medium (DMEM) with 10% fetal bovine

serum (FBS) and 1% penicillin-streptomycin antibiotics and maintained at 37 °C with 5% CO_2 incubator. The imHCs were developed by transfecting human mesenchymal stem cells with hTERT plus Bmi-1 and the cells were routinely characterized using a previous published protocol.[14] For 3D-monoculture spheroid generation, HepG2 or imHC were seeded at 1000 cells/well into an ultralow attachment 96-well plate. HSCs at 5%, 10%, and 15% were cocultured with HepG2 or imHC in the ULA plate to fabricate 3D coculture spheroid. The media was changed every 3–4 d after seeding. The spheroids were morphologically characterized over 14 d.

Assessment of Size, Morphology, and Cell Distribution within 3D-Liver Spheroids Using Immunofluorescence and Confocal Microscopy: The spheroids were morphologically characterized over a period of 14 d by a laser scanning confocal microscope (LSCM, Zeiss, Germany). To examine cell distribution using immunofluorescent staining, coculture spheroids were fixed and permeabilized with 4% paraformaldehyde and 0.1% Triton-X in PBS, respectively. The coculture spheroids were blocked with 1% BSA and 10% FBS in PBS for 1 h and incubated with primary antibodies including Cytokeratin-18 (CK18 (ab668), Abcam, Cambridge, UK) and Alexa Fluor 488 conjugated alpha-smooth muscle actin (α-SMA (sc53142), activated HSC biomarker; Santacruz, USA) at 4 °C for overnight. The samples were, then, rinsed several times with PBS before incubating with the secondary antibodies (Alexa Fluor 647 (ab150115), Abcam, Cambridge, UK) for 2 h. Next the samples were rinsed and mounted with mounting medium (ProLong Gold Antifade Mountant, ThermoFisher, USA) onto microscope slides with adhesive slide chamber. The 3D samples were imaged by LCMS (LSM 800, Zeiss, Germany). The stack images were analyzed using ZEISS ZEN (blue version 3.4, Germany) to observe cell distribution. Size and SI were measured using ImageJ software (version 1.8.0, USA)

Assessment of Protein Expression Using Immunofluorescence: Both mono and coculture spheroids were fixed and permeabilized with 4% paraformaldehyde and 0.1% Triton-X in PBS, respectively. The 3D-mono and coculture spheroids were blocked and incubated with primary antibodies including multi-drug resistance protein-2 (MRP2 (ab3373), Abcam, Cambridge UK), Collagen type 1 (COL1 (ab34710), Abcam, Cambridge, UK), Cytokeratin-18 (CK18 (ab668), Abcam, Cambridge, UK), Cytokeratin-19 with Alexa Fluor 488 (ab192643, Abcam, Cambridge, UK), and Zona Occludin1 (ZO1 (33-91000), Invitrogen, USA) as described in the previous section. The samples were rinsed several times with PBS before incubating with the secondary antibodies (except CK-19) for 2 h. Next the samples were rinsed and mounted with mounting medium. The 3D samples were visualized using LSCM (LSM 800, Zeiss, Germany). Laser intensity and detector gain of LCSM depended on antibodies; CK18 (1%, 700 V), MRP2 (2%, 800 V), CK19 (1%, 730 V), ZO-1 (3%, 800 V), and COL1 (0.7%, 760 V). The stack images were analyzed using ImageJ software (version 1.8.0, USA) and ZEISS ZEN (blue version 3.4, Germany). Mean fluorescent intensity (MFI) per area (mm^3) were calculated to compare the protein expression between mono and coculture models.

Assessment of O_2 Gradient: The solution of Image-iT Green hypoxia reagent was prepared following the manufacturing protocol. The hypoxia reagent stock solution was added to the cells at a final concentration of 5×10^{-6} M in the media; then the cells were incubated at 37 °C for 1 h for 3D spheroids. The culture media was changed to the fresh growth medium, then, the spheroids were incubated at 37 °C for 3 h. The 3D spheroids were imaged using LSCM (LSM 800, Zeiss, Germany). The stack images were analyzed using and ZEISS ZEN (blue version 3.4, Germany).

Assessment of Liver Functions and Liver Cancer Biomarkers Using ELISA: Supernatants of spheroids at day 5, 7, 10, and 14 were collected and stored at −80 °C until sample analysis. The amount of cancer biomarkers secreted into the culture media was measured by Milliplex Kit circulating cancer biomarkers according to the manufacturer's protocol (Merck, Germany). The quantity of albumin production within the culture media was determined by Human Serum Albumin DuoSet ELISA (R&D system, USA) following manufacturing protocol.

RNA Isolation: A pool of 3D-HepG2 and 3D-imHC spheroids of day 7, 10, and 14 was harvested and washed with PBS. Total ribonucleic acid (RNA) was extracted using Quick-RNA Microprep Kit (Zymo Research, USA) according to the manufacturers' protocol with an additional step of DNase I treatment to remove any contaminating deoxyribonucleic acid

Table 3. Primers used in this study.

Gene	Forward (5′–3′)	Reverse (5′–3′)
CYP1A2	ACCCCAGCTGCCCTACTTG	GCGTTGTGTCCCTTGTTGT
CYP2B6	CCTTCCTCTTCCAGTCCATTAC	GTTCAGCATCTTCAGGAACTCT
CYP2C8	ACAACAAGCACCACTCTGA-GATATG	GTCTGCCAATTACATGATCAATCTCT
CYP2C9	CCTCTGGGGCATTATCCATC	ATATTTGCACAGTGAAACATAGGA
CYP2C19	CAACAACCCTCGGGACTTTA	GTCTCTGTCCCAGCTCCAAG
CYP2D6	CATGGAGCTCTTCCTCTTCTTC	TCACCAGGAAAGCAAAGACA
CYP3A4	GCCTGGTGCTCCTCTATCTA	GGCTGTTGACCATCATAAAAGC
UGT1A4	CCTGCTGTGTTTTTTTGGAGGT	ATTGATCCCAAAGAGAAAACCAC
UGT2B4	TGGTGAGCTGCTGGCCGAGT	CATTGTCTCAAATAATGTAGTG
UGT2B7	GGAAATCATGTCAATATTTGG	CATTGTCTCAAATAATGTAGTG
GAPDH	GTCTCCTCTGACTTCAACAGCG	ACCACCCTGTTGCTGTAGCCAA

(DNA). RNA concentrations were determined with a NanoDrop OneC spectrophotometer (Thermo Scientific, USA) before performing quantitative RT-PCR.

Quantitative RT-PCR: Quantitative reverse transcription-polymerase chain reaction (qRT-PCR) was performed using the SYBR Green system. First strand complementary DNA (cDNA) synthesis was performed using 100 ng of RNA and iScript reverse transcription supermix (Bio-Rad, USA). Approximately 10 ng of first strand cDNA was used for qRT-PCR using Luna Universal qPCR Master Mix (NEB, USA) in triplicate on a C1000 Thermal Cycler (BioRad, USA) using a standard 40-cycle protocol. Primers used in this study are listed in **Table 3**.

Quantification of CYP450 Activities Using Liquid Chromatography-Mass Spectrometry/Mass Spectrometry (LC-MS/MS): Cells were routinely seeded to form spheroids using ULA technique as mentioned above. At day 10 after seeding, the spheroids were incubated with CYP450 probe cocktails consisting of three drugs including dextromethorphan (CYP2D6, 15×10^{-6} M), tolbutamide (CYP2C9, 500×10^{-6} M), and midazolam (CYP3A4, 10×10^{-6} M).[58] The supernatants were collected at time $t =$ 4, 24, 48, and 72 h after incubation. Samples spiked with acetonitrile containing an internal standard (IS), labetalol, for phase I metabolite analysis and 0.1% formic acid with acetonitrile containing diphenhydramine (IS) for phase II metabolite analysis. Spiked samples were vortexed thoroughly followed by centrifugation at 14000 g, 8 °C for 10 min. The supernatants were transferred into sample vials and injected to a LC-MS/MS system. The LC-MS/MS system consisted of an ExionLC UHPLC coupled with a Sciex QTRAP 6500+ hybrid triple-quadrupole linear ion trap mass spectrometer equipped with the ESI interface. All analytes were monitored in the positive mode except OH-tolbutamide which was detected in the negative mode. The mobile phase consisted of 0.1% formic acid in water and 0.1% formic acid in acetonitrile. The analytical column was Phenomenex Kinetex C18 (30 × 2.1 mm, 1.7 μm, Phenomenex, USA). The quantitative analysis was performed in the multiple reaction monitoring (MRM) mode. Two MRM transitions were monitored for each drug and drug metabolite. The transitions of the analytes and internal standard were m/z 272 → 171 and 147 for dextromethorphan, m/z 258 → 157 and 133 for dextrorphan, m/z 326 → 291 and 249 for midazolam, m/z 342 → 203 and 297 for OH-midazolam, m/z 518 → 324 and 342 for Midazolam 1′-O-glucuronide, m/z 271 → 91 and 172 for tolbutamide, m/z 285 → 186 and 104 for OH-tolbutamide, m/z 329 → 294 and 207 for labetalol, and m/z 256 → 167.2 and 165 for diphenhydramine. The most abundant product ion was used for quantification and the other was used for identification.[55,57]

Assessment of Anticancer Drug Penetration Using Live-Cell Imaging: Both 3D-HepG2 mono and coculture models were incubated with doxorubicin at concentration of 9.25 μg mL^{-1}. The 3D samples were imaged in real time by a LSCM (LSM 800, Zeiss, Germany). The imaging software ZEISS ZEN (blue version 3.4, Germany) was applied to analyze the penetration of doxorubicin into the internal core of spheroids.

Viability Assay: HepG2 was seeded at 1000 cells/well on an ultralow attachment 96-well plate. HSCs at 10% were cocultured with HepG2 in the

ULA plate to fabricate 3D coculture spheroid. The media was changed every 3–4 d after seeding. After 10 d the spheroids were exposed to serial concentrations, 1–600 μg mL^{-1}, of DOX for 24 h. Viability of 2D-HepG2 monoculture model was evaluated following 24 h exposure to DOX using WST-1 assays. The HepG2 cells were routinely seeded at 20000 cells/well and cultured into each well of a 96-well plate, in complete DMEM (GE Healthcare, USA), 10% fetal bovine serum (GE Healthcare, USA), and 1% penicillin-streptomycin (GE Healthcare, USA). At confluence, the cells were exposed to DOX at 37 °C with 5% CO_2 for 24 h.

Following 24 h exposure the exposure media was removed, and the fresh media contain WST-1 reagent (Sigma-Aldrich, USA). Spheroids were added and incubated for 1 h incubation (for 2D model) and 2 h incubation (for 3D models) at 37 °C with 5% CO_2. The supernatants were taken and add into the new 96-well flat bottom plate. The absorption was read at 480 nm using UV–vis spectrophotometer (Tecan, Switzerland). All experiments were done in triplicate ($n = 3$). The anticancer activity of DOX was calculated compared with the nontreated cells.

Statistical Analysis: All experiments were performed in triplicate ($n = 3$) and quadruplicate ($n = 4$; CYP450 gene expression at day 10). The results were expressed as mean $\pm$ standard deviation (SD) and mean $\pm$ standard error of the mean (SEM) in CYP450 gene expression study. The data were firstly tested by D'Agostino–Pearson normality test or Shapiro–Wilk normality test ($\alpha = 0.05$, $p > 0.05$) to confirm a normal distribution using Graph Pad Prism version 9.3.1. The data were, then, analyzed using two-way ANOVA with multiple comparison (Dunnett's test) and Kruskal–Wallis test with Dunnett's test to confirm differences, and the significant values were observed at ****$p < 0.0001$, ***$p < 0.005$, **$p < 0.05$, *$p < 0.05$, respectively. The letters **a** and **b** were used to represent significant difference between types of culture (monoculture vs coculture) and between period (day) of culture.

Supporting Information

Supporting Information is available from the Wiley Online Library or from the author.

Conflict of Interest

The authors declare no conflict of interest.

Author Contributions

P.R. conceived and designed the project. P.R., A.S., T.W., T.V., T.N., S.L., R.T., and A.J. performed the experiments. The manuscript was written by A.S. and P.R. and revised with T.W., T.V., K.S.-n., S.H., A.E.P., D.E., and K.S. with contributions from all authors. All authors discussed the results and commented on the manuscript. All authors have given approval to the final version of the manuscript.

Data Availability Statement

The data that support the findings of this study are available in the supplementary material of this article.

Keywords

[1] H. Sung, J. Ferlay, R. L. Siegel, M. Laversanne, I. Soerjomaaram, A. Jemal, F. Bray, *CA-Cancer J. Clin.* **2021**, *71*, 209.

[2] J. D. Yang, P. Hainaut, G. J. Gores, A. Amadou, A. Plymoth, L. R. Roberts, *Nat. Rev. Gastroenterol. Hepatol.* **2019**, *16*, 589.

[3] A. Mullard, *Nat. Rev. Drug Discovery* **2016**, *15*, 447.

[4] R. J. Weaver, E. A. Blomme, A. E. Chadwick, I. M. Copple, H. H. J. Gerets, C. E. Goldring, A. Guillouzo, P. G. Hewitt, M. Ingelman-Sundberg, K. G. Jensen, S. Juhila, U. Klingmüller, G. Labbe, M. J. Liguori, C. A. Lovatt, P. Morgan, D. J. Naisbitt, R. H. H. Pieters, J. Snoeys, B. van de Water, D. P. Williams, B. K. Park, *Nat. Rev. Drug Discovery* **2020**, *19*, 131.

[5] P. Godoy, N. J. Hewitt, U. Albrecht, M. E. Andersen, N. Ansari, S. Bhattacharya, J. G. Bode, J. Bolleyn, C. Borner, J. Böttger, A. Braeuning, R. A. Budinsky, B. Burkhardt, N. R. Cameron, G. Camussi, C. S. Cho, Y. J. Choi, J. C. Rowlands, U. Dahmen, G. Damm, O. Dirsch, M. T. Donato, J. Dong, S. Dooley, D. Drasdo, R. Eakins, K. S. Ferreira, V. Fonsato, J. Fraczek, R. Gebhardt, et al., *Arch. Toxicol.* **2013**, *87*, 1315.

[6] U.S. FDA, Drug Development and Drug Interactions: Table of Substrates, Inhibitors and Inducers, https://www.fda.gov/drugs/drug-interactions-labeling/drug-development-and-drug-interactions-table-substrates-inhibitors-and-inducers (accessed: October **2021**).

[7] C. C. Bell, A. C. A. Dankers, V. M. Lauschke, R. S. Young, R. Jenkins, C. Rowe, C. E. Goldring, K. Park, S. L. Regan, T. Walker, C. Schofield, A. Baze, A. J. Foster, D. P. Williams, A. W. M. van de Ven, F. Jacobs, J. van Houdt, T. Lähteenmäki, J. Snoeys, S. Juhila, L. Richert, M. I. Sundberg, *Toxicol. Sci.* **2018**, *162*, 655.

[8] R. Gupta, Y. Schrooders, D. Hauser, M. van Herwijnen, W. Albrecht, B. ter Braak, T. Brecklinghaus, J. V. Castell, L. Elenschneider, S. Escher, P. Guye, J. G. Hengstler, A. Ghallab, T. Hansen, M. Leist, R. Maclennan, W. Moritz, L. Tolosa, T. Tricot, C. Verfaillie, P. Walker, B. van de Water, J. Kleinjans, F. Caiment, *Arch. Toxicol.* **2021**, *95*, 573.

[9] F. Pampaloni, E. G. Reynaud, E. H. K. Stelzer, *Nat. Rev. Mol. Cell Biol.* **2007**, *8*, 839.

[10] S. U. Vorrink, Y. Zhou, M. Ingelman-Sundberg, V. M. Lauschke, *Toxicol. Sci.* **2018**, *163*, 655.

[11] C. C. Bell, D. F. G. Hendriks, S. M. L. Moro, E. Ellis, J. Walsh, A. Renblom, L. F. Puigvert, A. C. A. Dankers, F. Jacobs, J. Snoeys, R. L. Sison-Young, R. E. Jenkins, Å. Nordling, S. Mkrtchian, B. K. Park, N. R. Kitteringham, C. E. P. Goldring, V. M. Lauschke, M. Ingelman-Sundberg, *Sci. Rep.* **2016**, *6*, 25187.

[12] V. M. Lauschke, R. Z. Shafagh, D. F. G. Hendriks, M. Ingelman-Sundberg, *Biotechnol. J.* **2019**, *14*, 1800347.

[13] K. Takayama, M. Inamura, K. Kawabata, M. Sugawara, K. Kikuchi, M. Higuchi, Y. Nagamoto, H. Watanabe, K. Tashiro, F. Sakurai, T. Hayakawa, M. K. Furue, H. Mizuguchi, *J. Hepatol.* **2012**, *57*, 628.

[14] K. Sa-ngiamsuntorn, A. Wongkajornsilp, K. Kasetsinsombat, S. Duangsa-ard, L. Nuntakarn, S. Borwornpinyo, P. Akarasereenont, S. Limsrichamrern, S. Hongeng, *BMC Biotechnol.* **2011**, *11*, 89.

[15] K. Takayama, K. Kawabata, Y. Nagamoto, K. Kishimoto, K. Tashiro, F. Sakurai, M. Tachibana, K. Kanda, T. Hayakawa, M. K. Furue, H. Mizuguchi, *Biomaterials* **2013**, *34*, 1781.

[16] H. Ardalani, S. Sengupta, V. Harms, V. Vickerman, J. A. Thomson, W. L. Murphy, *Acta Biomater.* **2019**, *95*, 371.

[17] G. Lee, H. Kim, J. Y. Park, G. Kim, J. Han, S. Chung, J. H. Yang, J. S. Jeon, D. H. Woo, C. Han, S. K. Kim, H. J. Park, J. H. Kim, *Biomaterials* **2021**, *269*, 120529.

[18] B. Berger, M. Donzelli, S. Maseneni, F. Boess, A. Roth, S. Krähenbühl, M. Haschke, *Front. Pharmacol.* **2016**, *7*, 443.

[19] R. Negoro, M. Tasaka, S. Deguchi, K. Takayama, T. Fujita, *Mol. Cells* **2022**, *11*, 1677.

[20] S. C. Ramaiahgari, M. W. den Braver, B. Herpers, V. Terpstra, J. N. M. Commandeur, B. van de Water, L. S. Prince, *Arch. Toxicol.* **2014**, *88*, 1083.

[21] M. Štampar, J. Tomc, M. Filipič, B. Žegura, *Arch. Toxicol.* **2019**, *93*, 3321.

[22] Q. He, T. Okajima, H. Onoe, A. Subagyo, K. Sueoka, K. Kuribayashi-Shigetomi, *Sci. Rep.* **2018**, *8*, 4556.

[23] C. Eilenberger, M. Rothbauer, E. K. Ehmoser, P. Ertl, S. Küpcü, *Sci. Rep.* **2019**, *9*, 4863.

[24] Y. Song, S. H. Kim, K. M. Kim, E. K. Choi, J. Kim, H. R. Seo, *Sci. Rep.* **2016**, *6*, 36750.

[25] C. Yin, K. J. Evason, K. Asahina, D. Y. R. Stainier, *J. Clin. Invest.* **2013**, *123*, 1902.

[26] T. Tsuchida, S. L. Friedman, *Nat. Rev. Gastroenterol. Hepatol.* **2017**, *14*, 397.

[27] A. E. Barry, R. Baldeosingh, R. Lamm, K. Patel, K. Zhang, D. A. Domingue, K. J. Kirton, A. P. Shah, H. Dang, *Front. Cell Dev. Biol.* **2020**, *8*, 709.

[28] S. L. Friedman, *Physiol. Rev.* **2008**, *88*, 125.

[29] S. Khakpoura, A. D. Renzob, E. Curcioa, F. P. D. Maiob, L. Giornoa, L. D. Bartolo, *J. Membr. Sci.* **2017**, *544*, 312.

[30] Y. S. Weng, S. F. Chang, M. C. Shih, S. H. Tseng, C. H. Lai, *Adv. Mater.* **2017**, *29*, 1701545.

[31] M. Coll, L. Perea, R. Boon, S. B. Leite, J. Vallverdú, I. Mannaerts, A. Smout, A. E. Taghdouini, D. Blaya, D. Rodrigo-Torres, I. Graupera, B. Aguilar-Bravo, C. Chesne, M. Najimi, E. Sokal, J. J. Lozano, L. A. van Grunsven, C. M. Verfaillie, P. Sancho-Bru, *Cell Stem Cell* **2018**, *23*, 101.

[32] X. Zhai, W. Wang, D. Dou, Y. Ma, D. Gang, Z. Jiang, B. Shi, B. Jin, *Sci. Rep.* **2019**, *9*, 12757.

[33] M. Vinken, V. Rogiers, *Methods in Molecular Biology*, Springer, New York **2015**.

[34] R. M. Tostões, S. B. Leite, M. Serra, J. Jensen, P. Björquist, M. J. T. Carrondo, C. Brito, P. M. Alves, *Hepatology* **2012**, *55*, 1227.

[35] S. F. Wong, D. Y. No, Y. Y. Choi, D. S. Kim, B. G. Chung, S. H. Lee, *Biomaterials* **2011**, *32*, 8087.

[36] M. Zanoni, F. Piccinini, C. Arienti, A. Zamagni, S. Santi, R. Polico, A. Bevilacqua, *Sci. Rep.* **2016**, *6*, 19103.

[37] D. Hendriks, B. Artegiani, H. Hu, S. C. S. Lopes, H. Clevers, *Nat. Protoc.* **2021**, *16*, 182.

[38] P. Gissen, I. M. Arias, *J. Hepatol.* **2015**, *63*, 1023.

[39] W. Tang, Z. Chen, W. Zhang, Y. Cheng, B. Zhang, F. Wu, Q. Wang, S. Wang, D. Rong, F. P. Reiter, E. N. D. Toni, X. Wang, *Signal Transduction Targeted Ther.* **2020**, *5*, 87.

[40] J. J. G. Marin, M. J. Monte, R. I. R. Macias, M. R. Romero, E. Herraez, M. Asensio, S. Ortiz-Rivero, C. Cives-Losada, S. D. Giacomo, J. Gonzalez-Gallego, J. L. Mauriz, T. Efferth, O. Briz, *Cancers* **2022**, *14*, 3524.

[41] J. M. Pedersen, P. Matsson, C. A. S. Bergström, U. Norinder, J. Hoogstraate, P. Artursson, *J. Med. Chem.* **2008**, *51*, 3275.

[42] X. R. Yang, Y. Xu, G. M. Shi, J. Fan, J. Zhou, Y. Ji, H. C. Sun, S. J. Qiu, B. Yu, Q. Gao, Y. Z. He, W. Z. Qin, R. X. Chen, G. H. Yang, B. Wu, Q. Lu, Z. Q. Wu, Z. Y. Tang, *Clin. Cancer Res.* **2008**, *14*, 3850.

[43] European Association for the Study of the Liver (EASL), *J. Hepatol.* **2018**, *69*, 182.

[44] J. Zhuo, D. Lu, Z. Lin, X. Yand, M. Yang, J. Wang, Y. Tao, X. Wen, H. Li, Z. Lian, B. Cen, S. Dong, X. Wei, H. Xie, S. Zheng, Y. Shen, X. Xu, *Cell Death Dis.* **2021**, *12*, 1084.

[45] M. B. Zeisel, P. Dhawan, T. F. Baumert, *Gut* **2019**, *68*, 547.

[46] A. M. Ortega-Prieto, J. K. Skelton, S. N. Wai, E. Large, M. Lussignol, G. Vizcay-Barrena, D. Hughes, R. A. Fleck, M. Thursz, M. T. Catanese, M. Dorner, *Nat. Commun.* **2018**, *9*, 682.

[47] F. Tonon, G. G. Giobbe, A. Zambon, C. Luni, O. Gagliano, A. Floreani, G. Grassi, N. Elvassore, *Sci. Rep.* **2019**, *9*, 13557.

[48] N. Berndt, E. Kolbe, R. Gajowski, J. Eckstein, F. Ott, D. Meier-hofer, H. G. Holzhütter, M. Matz-Soja, *Hepatology* **2021**, *73*, 795.

[49] S. Ben-Moshe, S. Itzkovitz, *Nat. Rev. Gastroenterol. Hepatol.* **2019**, *16*, 395.

[50] W. Senkowski, X. Zhang, M. H. Olofsson, R. Isacson, U. Höglund, M. Gustafsson, P. Nygren, S. Linder, R. Larsson, M. Fryknäs, *Mol. Cancer Ther.* **2015**, *14*, 1504.

[51] M. Singh, S. Mukundan, M. Jaramillo, S. Oesterreich, S. Sant, *Cancer Res.* **2016**, *76*, 3732.

[52] M. Vinci, S. Gowan, F. Boxall, L. Patterson, M. Zimmermann, W. Court, C. Lomas, M. Mendiola, D. Hardisson, S. A. Eccles, *BMC Biol.* **2012**, *10*, 29.

[53] Y. Duan, J. Zhu, J. Yang, G. Liu, X. Bai, N. Qu, X. Wang, X. Li, *Front. Pharmacol.* **2020**, *11*, 574176.

[54] N. Handin, E. Mickols, M. Ölander, J. Rudfeldt, K. Blom, F. Nyberg, W. Senkowski, J. Urdzik, V. Maturi, M. Fryknäs, P. Artursson, *iScience* **2021**, *24*, 103235.

[55] F. G. M. Russel, *Enzyme- and Transporter-Based Drug-Drug Interactions*, Springer, New York **2010**.

[56] K. A. Seo, S. K. Bae, Y. K. Choi, C. S. Choi, K. H. Liu, J. G. Shin, *Drug Metab. Dispos.* **2010**, *38*, 2007.

[57] R. Hyland, T. Osborne, A. Payne, S. Kempshall, Y. R. Logan, K. Ezzeddine, B. Jones, *Br. J. Clin. Pharmacol.* **2009**, *67*, 445.

[58] R. L. Walsky, R. S. Obach, *Drug Metab. Dispos.* **2004**, *32*, 647.

[59] S. U. Vorrink, S. Ullah, S. Schmidt, J. Nandania, V. Velagapudi, O. Beck, M. Ingelman-Sundberg, V. M. Lauschke, *FASEB J.* **2017**, *31*, 2696.

[60] S. Koyama, H. Arakawa, M. Itoh, N. Masuda, K. Yano, H. Kojima, T. Ogihara, *Biopharm. Drug Dispos.* **2018**, *39*, 187.

[61] D. R. Berger, B. R. Ware, M. D. Davidson, S. R. Allsup, S. R. Khetani, *Hepatology* **2015**, *61*, 1370.

[62] H. Rashidi, N. T. Luu, S. M. Alwahsh, M. Ginai, S. Alhaque, H. Dong, R. A. Tomaz, B. Vernay, V. Vigneswara, J. M. Hallett, A. Chandrashekran, A. Dhawan, L. Vallier, M. Bradley, A. Callanan, S. J. Forbes, P. N. Newsome, D. C. Hay, *Arch. Toxicol.* **2018**, *92*, 3117.

[63] A. X. Zhu, D. G. Duada, D. V. Sahani, R. K. Jain, *Nat. Rev. Clin. Oncol.* **2011**, *8*, 292.

[64] J. M. Llovet, J. Zucman-Rossi, E. Pikarsky, B. Sangro, M. Schwartz, M. Sherman, G. Gores, *Nat. Rev. Dis. Primers* **2016**, *2*, 16018.

[65] J. M. Llovet, R. K. Kelley, A. Villanueva, A. G. Singal, E. Pikarsky, S. Roayaie, R. Lencioni, K. Koike, J. Zucman-Rossi, R. S. Finn, *Nat. Rev. Dis. Primers* **2021**, *7*, 6.

[66] M. D. Giraldez, D. Carneros, C. Garbers, S. Rose-John, M. Bustos, *Nat. Rev. Gastroenterol. Hepatol.* **2021**, *18*, 787.

[67] C. Porta, M. De Amici, S. Quaglini, C. Paglino, F. Tagliani, A. Boncimino, R. Moratti, G. R. Corazza, *Ann. Oncol.* **2008**, *19*, 353.

[68] I. A. Khawar, J. K. Park, E. S. Jung, M. A. Lee, S. Chang, H. J. Kuh, *Neoplasia* **2018**, *20*, 800.

2200169 (16 of 16)